metals

MDPI

Article

Avrami Kinetic-Based Constitutive Relationship for Armco-Type Pure Iron in Hot Deformation

Yan Zhang, Qichao Fan *, Xiaofeng Zhang, Zhaohui Zhou, Zhihui Xia and Zhiqiang Qian

Institute of Machinery Manufacturing Technology, Chinese Academy of Engineering Physics, Mianyang 621900, China; zhangyan_19860920@126.com (Y.Z.); zfx1999984@163.com (X.Z.); zhouzh2001@sina.com (Z.Z.); xiazhihui@caep.cn (Z.X.); qianzhiqiang@caep.cn (Z.Q.)

* Correspondence: fanqichao@126.com or fanqichao@caep.cn; Tel.: +86-816-248-5668; Fax: +86-816-248-7614

Received: 2 March 2019; Accepted: 16 March 2019; Published: 21 March 2019

Abstract: The work presents a full mathematical description of the stress-strain compression curves in a wide range of strain rates and deformation temperatures for Armco-type pure iron. The constructed models are based on a dislocation structure evolution equation (in the case of dynamic recovery (DRV)) and Avrami kinetic-based model (in the case of dynamic recrystallization (DRX)). The fractional softening model is modified as: $X = (\sigma^2 - \sigma_r^2)/(\sigma_{ds}^2 - \sigma_r^2)$ considering the strain hardening of un-recrystallized regions. The Avrami kinetic equation is modified and used to describe the DRX process considering the strain rate and temperature. The relations between the Avrami constant k^*, time exponent n^*, strain rate $\dot{\varepsilon}$, temperature T and Z parameter are discussed. The yield stress σ_y, saturation stress σ_{rs}, steady stress σ_{ds} and critical strain ε_c are expressed as the functions of the Z parameter. A constitutive model is constructed based on the strain-hardening model, fractional softening model and modified Avrami kinetic equation. The DRV and DRX characters of Armco-type pure iron are clearly presented in these flow stress curves determined by the model.

Keywords: Avrami kinetic; constitutive model; dynamic recovery; dynamic recrystallization; hot deformation; pure iron

1. Introduction

The hot deformation process (e.g., forging and sheeting) is crucial for the industrial use of alloys to refine the grains, eliminate the defects and change the shape. To better control and simulate the deforming process, the flow behavior of alloys in hot deformation should be well described. Flow behavior is mainly affected by the deformation temperature, strain rate, strain, inner microstructure and chemical composition [1–3]. In previous studies, various constitutive relationships have been constructed to describe the flow behavior during the hot deformation process, which are introduced as follows:

Zener and Hollomon suggested that the isothermal stress-strain relation in steels depends on the strain rate $\dot{\varepsilon}$, temperature T and activation energy Q, and meanwhile concluded that the logarithm of the flow stress σ is a linear function of the logarithm of the Zener-Holloman parameter (Z parameter) which has the form: $Z = \dot{\varepsilon}\exp(Q/RT)$. The Z parameter depicts the combined effect of $\dot{\varepsilon}$ and T on the constitutive relationship in a simple form and is generally used to describe the hot deformation behaviors of alloys [4].

Johnson and Cook described the flow behavior, considering the effects of strain hardening, strain rate hardening and thermal softening separately, and proposed the Johnson-Cook (JC) model [5]. The JC model has been widely used to describe the constitutive relations of alloys, because the material constants can be easily determined from a limited straining test done in torsion, tension and compression. For example, Ulacia et al. and Bhattacharya et al. used modified JC models to predict

the flow behavior of an aAZ31 magnesium alloy at an elevated temperature [6,7]. Meanwhile, several calibration strategies for the JC model were proposed and clearly discussed by Gambirasio et al. [8]. Basing on dislocation mechanics, Zerilli et al. proposed the Zerilli-Armstrong (ZA) model with two different forms to separately describe the constitutive relationships of the fcc structure and bcc structure [9]. The dislocation-based model is intimately linked to the actual physical process, as compared to the JC model, and offers the possibility of accurately describing the constitutive relations. However, the restrained structure and the complicated regression process limit the use of the ZA model. In addition, Estrin and Mecking proposed the Estrin-Mecking (EM) model, based on the evolution of the dislocation density from work hardening and dynamic recovery (DRV) [10]. The EM model describes the flow curves up to the peak stress, and has been widely used to study the flow and work hardening behavior of steels [11–13]. For example, Haghdadi et al., Choudhary et al. and Chalimba et al. used the model to describe the deformation behavior of LDX 2101 duplex stainless steel, chromium ferritic-martensitic steel and V-Nb-alloyed steel, respectively.

The Arrhenius-type model with sine-hyperbolic law was first proposed by Sellars et al., in which the flow stress is expressed by a sine hyperbolic in an Arrhenius-type equation [14]. Among the constitutive models mentioned above, the Arrhenius-type model with sine-hyperbolic law has been successfully and widely applied for predicting the flow behavior of alloys in a hot deformation. For example, Liu et al., Tabei et al. and Zhang et al. used the model to describe the flow behavior of the 316LN alloy, Ti-6Al-4V alloy and 6N01 aluminum alloy at elevated temperatures, respectively [15–17]. Although widely used in the hot deformation area, the strain effects on flow behavior are not considered in the model, which reduces the accuracy in some conditions.

The hot deformation process is usually accompanied by dynamic recrystallization (DRX) due to its high temperature and stored energy. According to the research results of Kugler et al. and Martin et al., the newly formed grains in DRX play an important role in the material flow behavior [18,19]. In order to accurately describe the flow behavior in hot deformation, DRX should be considered. However, DRX is neglected in all of the above discussed constitutive relationships due to its complicated process. In this paper, a constitutive model only relating to the DRV process is constructed from the Kocks-Mecking (KM) model and used to describe the strain-hardening process of Armco-type pure iron before the initiation of DRX. Meanwhile, the Avrami kinetic equation is discussed and modified to describe the kinetics of the DRX process considering the effects of strain rate and temperature. At last, the Avrami kinetic-based constitutive model considering the effects of DRV and DRX is constructed and used to describe the flow behavior of Armco-type pure iron in hot deformation.

2. Materials and Experimental Details

The exact chemical compositions of Armco-type pure iron used for investigations are shown in Table 1. The initial grain size of Armco-type pure iron is about 100 μm. Cylindrical compression samples with an 8 mm in diameter and 12 mm length were prepared by an electro-discharge machine DK7720, and the surfaces of these samples were finely polished with diamond pastes. Hot compression tests relating to DRX were performed on a Gleeble-1500 thermal-mechanical simulator with strain rates of 0.001 s^{-1}, 0.01 s^{-1}, 0.1 s^{-1} and 1 s^{-1} at temperatures of 1273 k–1473 k, while warm compression tests relating to only DRV were also performed on the simulator with a strain rate of 1 s^{-1} at temperatures of 973 k and 1023 k for Armco-type pure iron. Quartz plates were stuck on samples to reduce the friction during compression. The samples were heated to corresponding temperatures and kept for 3 minutes to ensure that the temperature uniformly distributed. The decrease in height was 60% at the end of the compression tests, after which these samples were quenched in water. The compressed samples were sectioned along the center axis by electro-spark wire-electrode cutting, then polished and chemically etched in a solution of 5% nitric acid and 95% alcohol to reveal the grain boundaries. The optical microstructures of these samples were observed by an optical microscope (Axio Observer A1m).

Table 1. The chemical composition of Armco-type pure iron (at.%).

C	Si	Mn	P	S
0.0019	0.0294	0.1298	0.0056	0.0038

3. Analysis Methods

In order to unify all the experimental curves and fully avoid the influence of the elastic stage, the yield stress was identified in terms of a 1% offset in the whole strain, which is larger than the widely used value of 0.2%. After the removal of the elastic portion, the yield strain ε_y was defined as zero in these true stress-strain curves. All of true stress-strain curves that were obtained from the compression tests were employed for the analysis. Each curve was fitted and smoothed with a tenth-order polynomial using the MatLab 7.0 software. The polynomial fitting eliminated the irregularities and fluctuations of experimental curves and then permitted the differentiations used later. After the polynomial fitting, some original values of true stress-strain curves for Armco-type pure iron were chosen and are presented in the Supplementary Materials of Table S1.

4. Flow Behavior and Microstructure Evolvement

At the beginning of the hot deformation process, strain hardening initiates, which refers to the storage and annihilation (rearrangement) of dislocations [20]. Here the annihilation process is a dynamic recovery. The DRX process initiates when the dislocation density reaches an sufficient level to permit the nucleation of new grains. The new grains produce a softening and then decrease the work-hardening rate until eventually there is a clear stress peak. As volume fraction of new grains increases, more and more softening happens, and the flow stress decreases. After all the original microstructures transform into new grains, the strain hardening and strain softening reach a dynamic equilibrium, and then a steady state of flow stress appears [21,22]. According to the evolvement of the microstructure, the true stress-strain curve (σ) is divided into three different parts: part I, part II and part III, and the schematic curve is shown in Figure 1. Here, part I is supposed to be the strain-hardening process before the DRX initiation. Micro-bands (MBs) usually appear in the austenite structure at this stage, which are formed by multiple cross-slips of dislocations or dislocation wall splitting [23,24]. Part II is the initiation of the DRX process, where the original microstructure transforms into new grains. The DRX process is supposed to be discontinuous in the austenite structure because of its low stacking fault energy, which inhibits DRV. The DRX grains in the austenite tend to nucleate through strain-induced boundary migration, e.g., the bulging of original grain boundaries, often accompanied by twinning [23,24]. Part III is supposed to be a steady state. As shown in the figure, DRX initiates at the critical strain ε_c and critical stress σ_c where part I changes to part II, peak strain ε_p and peak stress σ_p are supposed to be the point where $d\sigma/d\varepsilon$ falls to zero in part II, and σ_{ds} is the steady stress which can also be determined from these points where $d\sigma/d\varepsilon$ is equal to zero in part III. The typical true stress-strain curves relating to DRX are presented in Figure 2a,b, and the grains corresponding to the steady state are isometric crystal, which is the typical microstructure of completed DRX.

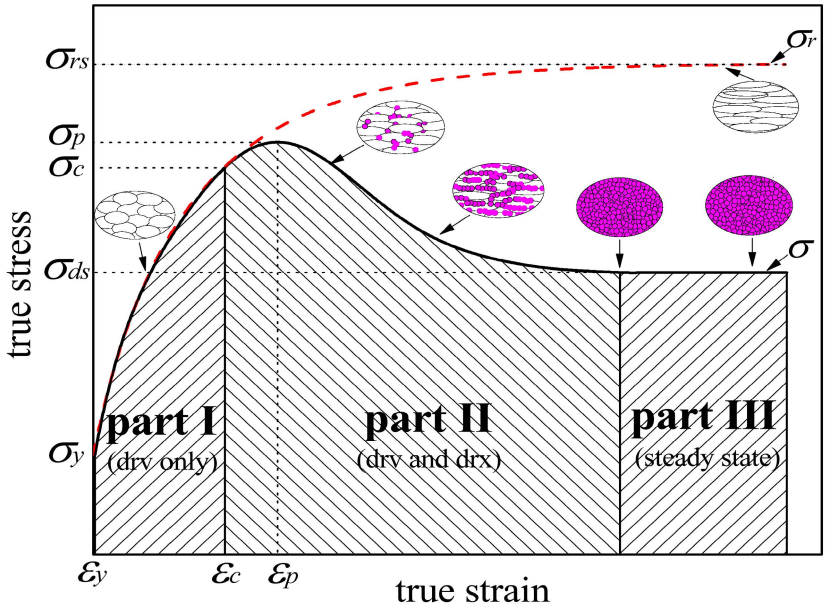

Figure 1. Schematic illustration of the microstructure evolvement and the division of the true stress-strain curve in the hot deformation process. According to the difference of the microstructure evolvement, the true stress-strain curve (σ) is divided into three parts (part I, part II and part III). Part I undergoes the dynamic recovery (DRV) process. Part II is the initiation of the dynamic recrystallization (DRX) process while these un-recrystallized regions still undergo the DRV process. Part III is the steady state; all the original microstructure has been recrystallized and reaches a dynamic equilibrium in this part. The dashed curve (σ_r) represents the work-hardening behavior of part I and the un-recrystallized regions in part II.

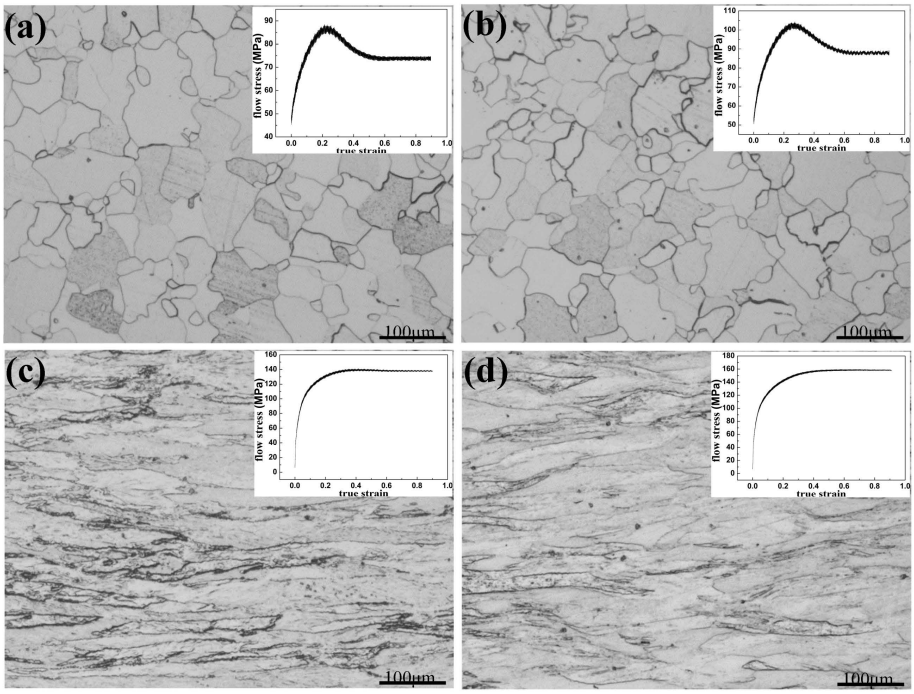

Figure 2. Microstructure of Armco-type pure iron deformed at different conditions: (**a**) $\dot{\varepsilon}$ = 1s^{-1}, T = 1423K; (**b**) $\dot{\varepsilon}$ = 1s^{-1}, T = 1373K; (**c**) $\dot{\varepsilon}$ = 1s^{-1}, T = 1023K; and (**d**) $\dot{\varepsilon}$ = 1s^{-1}, T = 973K. (**a**,**b**) relate to the completed DRX process in the hot deformation, while (**c**,**d**) relate to the DRV process with the deformation temperature lower than that of the hot deformation. The inserted figures are the corresponding true stress- strain cures.

Shown in Figure 1, the dashed curve (σ_r) is supposed to be the one that resulted only from the restoration process of DRV, i.e., in the absence of DRX. It represents the assumed strain-hardening behavior of part I and the un-recrystallized regions in part II. Although it cannot be directly obtained from experiments related to DRX, this curve can be derived from the strain-hardening behavior of part I. In the dashed curve, the saturation state is attained when the dislocation annihilation has increased sufficiently to balance the dislocation storage, and then the stress (σ_{rs}) reaches a steady value. As shown in Figure 2c,d, the typical true stress-strain curves only relating to DRV are presented with low deformation temperatures, and the grains corresponding to the saturation state of these curves are elongated along the deformation direction, which is the typical microstructure with only the DRV process.

5. Constitutive Relationship in Hot Deformation

5.1. Constitutive Relationship of Part I

5.1.1. Constitutive Models Only Relating to DRV Process

When deformed in part I, the strain-hardening process is controlled by the competition of the storage and annihilation of dislocations. These two processes are supposed to superimpose in an opposite manner. In the KM model, the relation between the dislocation density ρ_r and plastic strain ε is expressed as follows [10]:

$$\frac{d\rho_r}{d\varepsilon} = k_1 - k\rho_r \tag{1}$$

where k_1 is an athermal constant associated with the storage process, $k\rho_r$ is associated with the annihilation (DRV) process, and $k = k(\dot{\varepsilon}, T)$. Though the integration of Equation (1), the following equation can be obtained:

$$\rho_r = \frac{k_1}{k} - \frac{C}{k}\exp(-k\varepsilon) \tag{2}$$

Because ε_y was defined as zero, C can be derived as: $k_1 - k\rho_y$. Then, Equation (2) can be expressed as follows:

$$\rho_r = \rho_y \exp(-k\varepsilon) + \frac{k_1}{k}[1 - \exp(-k\varepsilon)] \tag{3}$$

As shown in the dashed curve of Figure 1, $d\rho_r/d\varepsilon = 0$ when in the saturation process. Therefore, according to Equation, (1), $\rho_{rs} = k_1/k$. Then, Equations (1) and (3) can be expressed as follows:

$$\frac{d\rho_r}{d\varepsilon} = k(\rho_{rs} - \rho_r) \tag{4}$$

$$\rho_r = \rho_y \exp(-k\varepsilon) + \rho_{rs}[1 - \exp(-k\varepsilon)] \tag{5}$$

The relation between σ and the dislocation density ρ is expressed as follows by [10]:

$$\sigma = a^* G b \rho^{1/2} \tag{6}$$

Therefore, ρ_r, ρ_{rs} and ρ_y in Equations (4) and (5) can be replaced by $(\sigma_r/a^*Gb)^2$, $(\sigma_{rs}/a^*Gb)^2$, and $(\sigma_y/a^*Gb)^2$, respectively. In this way, Equations (4) and (5) can be rewritten as follows:

$$\frac{d{\sigma_r}^2}{d\varepsilon} = k(\sigma_{rs}^2 - {\sigma_r}^2) \tag{7}$$

$${\sigma_r}^2 = \sigma_y^2 \exp(-k\varepsilon) + \sigma_{rs}^2[1 - \exp(-k\varepsilon)] \tag{8}$$

As shown in Equation (8), this constitutive model presents the mathematic expression of the dashed line shown in Figure 1, and describes the constitutive relationships of part I and the un-recrystallized regions in part II.

5.1.2. Determination of Constant k

According to Equation (7), $d\sigma_r{}^2/d\varepsilon$ presents a linear relation with $\sigma_r{}^2$. Meanwhile, through the linear regression of $d\sigma_r{}^2/d\varepsilon$ vs. $\sigma_r{}^2$, k is obtained as the slope and σ_{rs} can be calculated from the intercept. The relation between $d\sigma^2/d\varepsilon$ and σ^2 of Armco-type pure iron is presented in Figure 3. As shown in the figure, the fitting linear curves before the DRX critical points are employed to determine the values of k and σ_{rs} for different temperatures and strain rates, and these calculated values are shown in the Supplementary Materials of Table S2. Based on the calculated values of k, σ_{rs} and the fitted values of σ_y, the flow stress curves only relating to the DRV process for Armco-type pure iron are calculated out through Equation (8) and presented in Figure 4. As discussed above, these flow stress curves stand for the work-hardening behavior of part I and the un-recrystallized regions in part II. As shown in Figure 4, these calculated curves fit well with the original true stress-strain curves in part I. Therefore, the flow behavior of part I with only the DRV process can be well described through Equation (8).

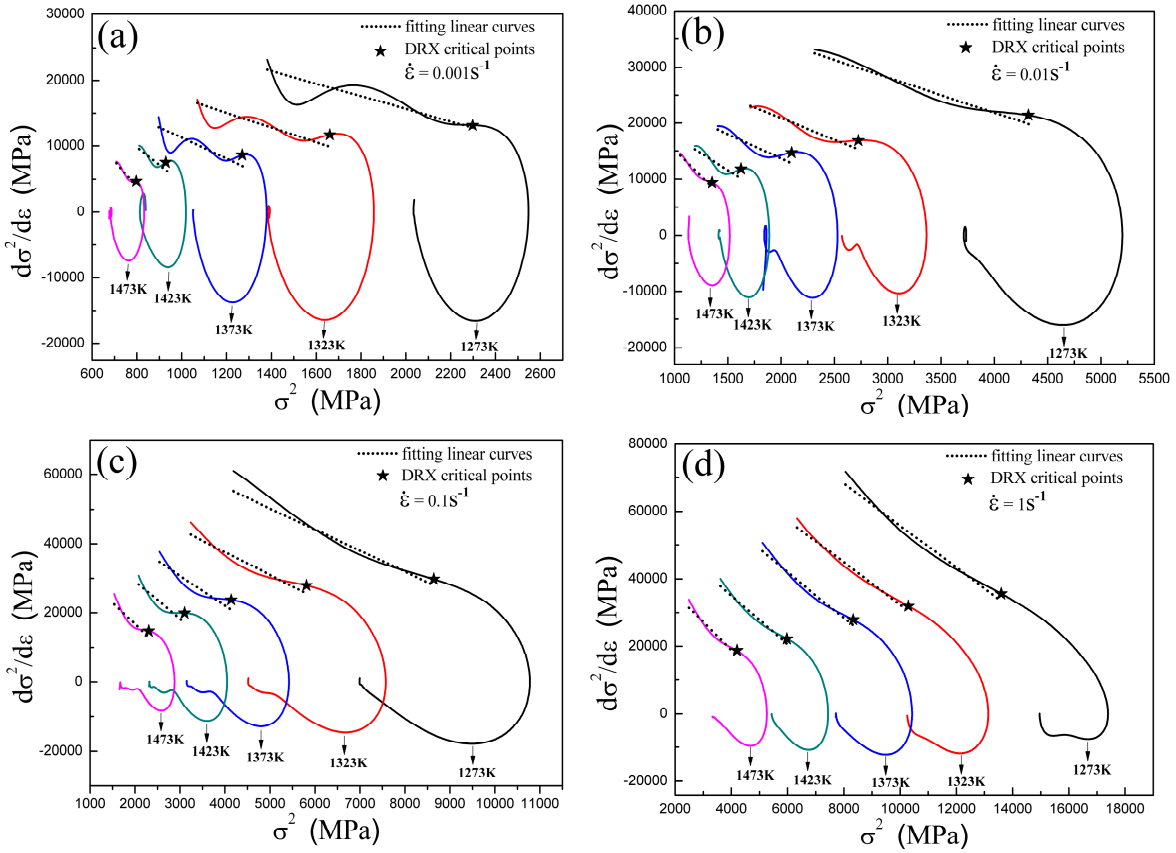

Figure 3. $d\sigma^2/d\varepsilon$ vs. σ^2 plots derived from the true stress-strain curves of Armco-type pure iron: (**a**) $\dot{\varepsilon}$ = 0.001 s^{-1}; (**b**) $\dot{\varepsilon}$ = 0.01 s^{-1}; (**c**) $\dot{\varepsilon}$ = 0.1 s^{-1}; and (**d**) $\dot{\varepsilon}$ = 1 s^{-1}. The part before the DRX critical point of each curve refers to the DRV process and is fitted by the linear curve of the dot line. These linear curves are employed to determine the values of k and σ_{rs}. The method to determine the DRX critical points will be discussed later.

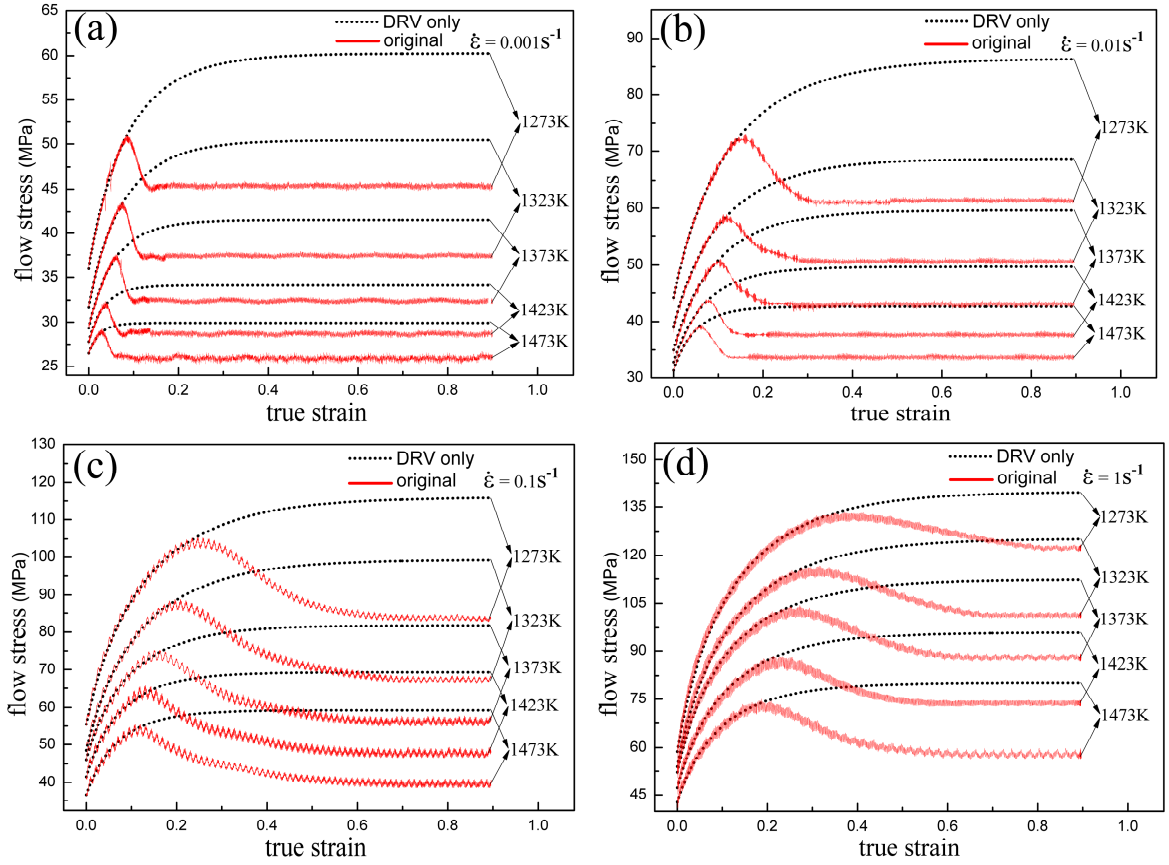

Figure 4. Original true stress-strain curves and calculated flow stress curves considering only the DRV process of Armco-type pure iron: (**a**) $\dot{\varepsilon}$ = 0.001 s^{-1}; (**b**) $\dot{\varepsilon}$ = 0.01 s^{-1}; (**c**) $\dot{\varepsilon}$ = 0.1 s^{-1}; and (**d**) $\dot{\varepsilon}$ = 1 s^{-1}. The red solid curves are the original true stress-strain curves while the dot lines are the curves calculated through Equation (8). The dot lines describe the work-hardening behavior of part I and the un-recrystallized regions in part II.

As presented in Equation (1), k is the function of $\dot{\varepsilon}$ and T. In order to completely describe the flow behavior of DRV, it is crucial to determine the equation of $k = k(\dot{\varepsilon}, T)$. According to Zener et al., $\dot{\varepsilon}$ and T usually show combined effects on hot deformation in the form of the Z parameter [4]. Whether $\dot{\varepsilon}$ and T show combined effects (e.g., in the form of the Z parameter) or individual effects on k should be discussed. Therefore, the $\ln Z$ vs. $\ln k$ curve shown in Figure 5 is employed to determine the relationship between the Z parameter and k. Through polynomial fitting, the relation between the Z parameter and k can be expressed as follows:

$$\ln k = 0.01723(\ln Z)^2 - 1.18699(\ln Z) + 22.28195 \quad (9)$$

As shown in Equation (9), $\dot{\varepsilon}$ and T present the combined effects on k in the form of the Z parameter.

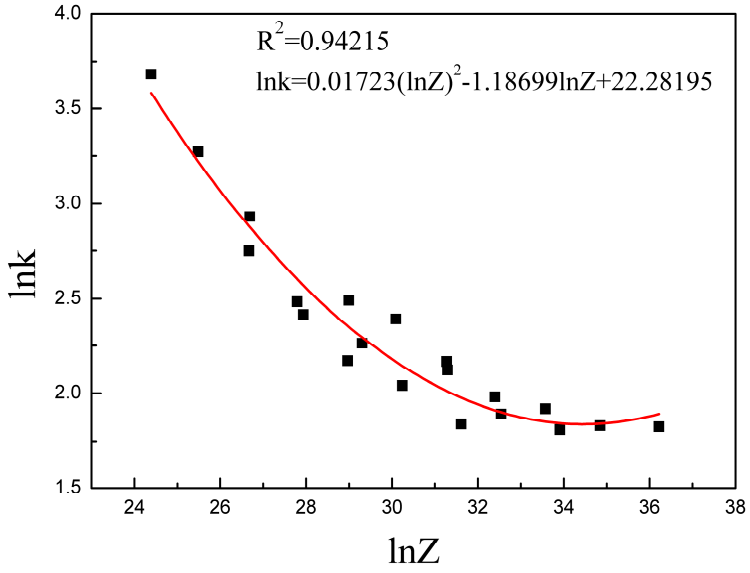

Figure 5. The relationship between the Z parameter and k. The curve is obtained from polynomial fitting in the order of two. Here, the Z parameter is in the form of $Z = \dot{\varepsilon}\exp(383094/(8.31T))$ which is calculated in following chapter.

5.2. Constitutive Relationship of Part II

5.2.1. Avrami Kinetic Equation for DRX

The Avrami kinetic equation first proposed by Avrami has been widely used to describe the static recrystallization (SRX) process [25,26]. Although originally intended to quantify the progress of the recrystallized volume fraction, it has also been employed to describe the fractional softening later in the SRX process. The Avrami kinetic equation for SRX is usually expressed as follows:

$$X = 1 - \exp(-k^* t^{n^*}) \tag{10}$$

Through some appropriate modifications, Equation (10) was used to describe the case of DRX by Jonas et al., Kim et al. and Quan et al. [27–29]. However, among these former modifications, the modified equations are not as accurate as is expected, or their expressions are very complicated. For example, Jonas et al. modified the Avrami equation as: $X = 1 - \exp\left[-0.693(t/t_{50})^{n^*}\right]$, where t_{50} is given by the expression of $t_{50} = A'\dot{\varepsilon}^{-q}d^{v}\exp(Q/RT)$ [27]. The expression is very complicated; therefore, it is very hard to determine the constants; additionally, its reliability also has not been clearly discussed. Kim et al. simplified the Avrami equation as: $X = 1 - \exp\left[-((\varepsilon - \varepsilon_c)/\varepsilon^*)^{n^*}\right]$, where ε^* is the strain corresponding to the maximum softening rate [28]. The simplification promotes the application of Avrami kinetics to DRX, however, the accuracy is limited due to the neglect of the Avrami constant k^*. In this paper, the original Avrami equation of Equation (10) is chosen to describe the volume fraction of recrystallized microstructures during the DRX process. Hot deformation usually refers to different temperatures and strain rates. Therefore, k^* and n^* are supposed to be the functions of T and $\dot{\varepsilon}$ when using Equation (10) for the DRX process. DRX initiates at the critical strain, so t for DRX can be replaced by: $(\varepsilon - \varepsilon_c)/\dot{\varepsilon}$. According to these modifications, Equation (10) can be used to describe the DRX process, and the modified equation is expressed as follows:

$$X = 1 - \exp\left[-k^*\left(\frac{\varepsilon - \varepsilon_c}{\dot{\varepsilon}}\right)^{n^*}\right] \tag{11}$$

where $k^* = k^*(\dot{\varepsilon}, T)$ and $n^* = n^*(\dot{\varepsilon}, T)$.

5.2.2. Determination of Critical Strain ε_c

The DRX process initiates at the critical strain where part I changes to part II. Poliak et al. proposed that the critical state for the onset of DRX corresponds to an inflection point in the θ vs. σ curve [30]. Here θ is the work-hardening rate and expressed as: $\theta = \partial\sigma/\partial\varepsilon$. According to mathematics, the inflection point corresponds to the peak point of the $-\partial\theta/\partial\sigma$ vs. σ curve. Therefore, in order to determine the critical state for Armco-type pure iron at different temperatures and strain rates, $-\partial\theta/\partial\sigma$ vs σ curves are calculated out and presented in Figure 6. As shown in the figure, σ_c is very close to σ_p, and the values are determined from the peak points of each curve. After determining σ_c, the corresponding ε_c can be obtained from the original true stress-strain curves, the values of which are shown in the Supplementary Materials of Table S2. Figure 7 presents the relationship between ε_c and the Z parameter. As shown in this figure, $\ln\varepsilon_c$ and $\ln Z$ present a linear relation. Through linear fitting, ε_c is expressed in the function of the Z parameter as follows:

$$\varepsilon_c = 2.74264 \times 10^{-4} Z^{0.18138} \quad (12)$$

As shown in Equation (12), $\dot{\varepsilon}$ and T also present combined effects on ε_c in the form of the Z parameter.

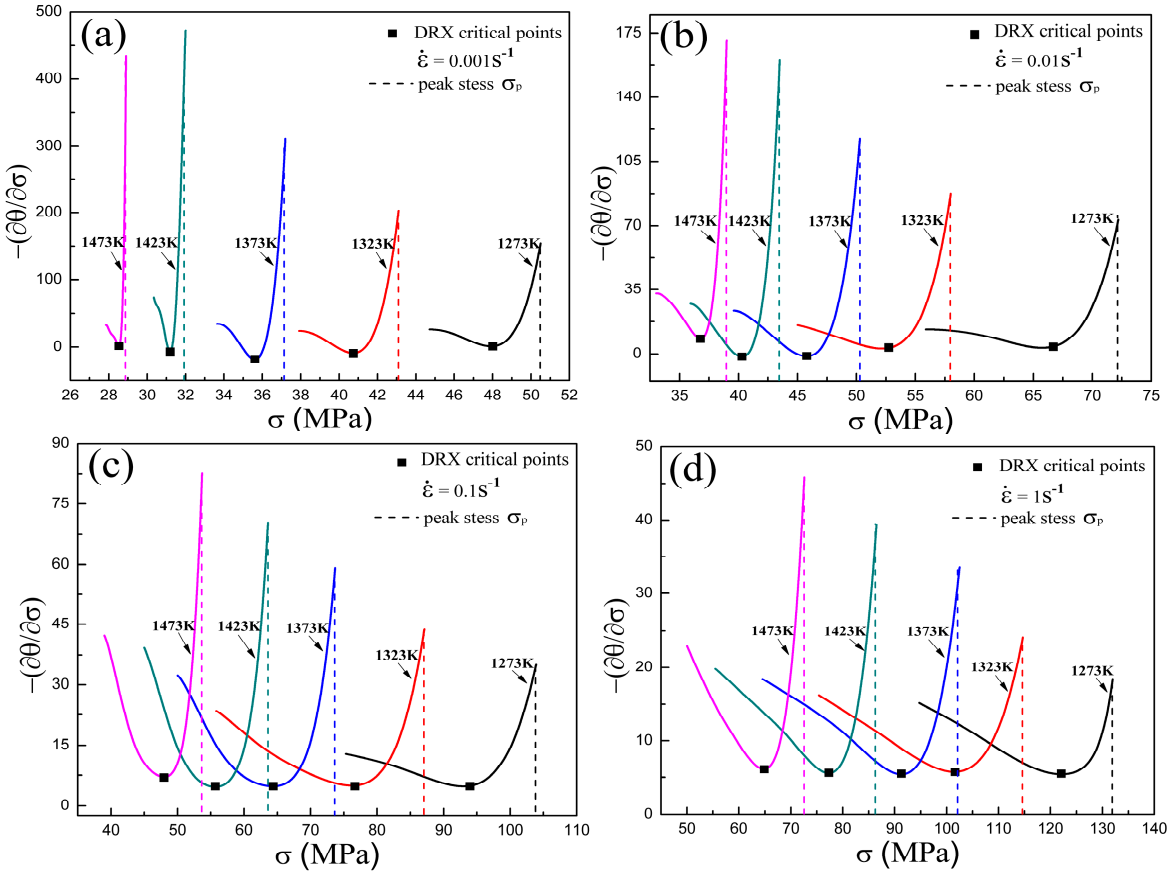

Figure 6. $-\partial\theta/\partial\sigma$ vs. σ curves of Armco-type pure iron: (**a**) $\dot{\varepsilon} = 0.001\ s^{-1}$; (**b**) $\dot{\varepsilon} = 0.01\ s^{-1}$; (**c**) $\dot{\varepsilon} = 0.1\ s^{-1}$; and (**d**) $\dot{\varepsilon} = 1\ s^{-1}$. According to the Poliak method, the DRX critical point is supposed to be the peak point of each curve [30]. The dashed lines correspond to the peak stresses of each curve.

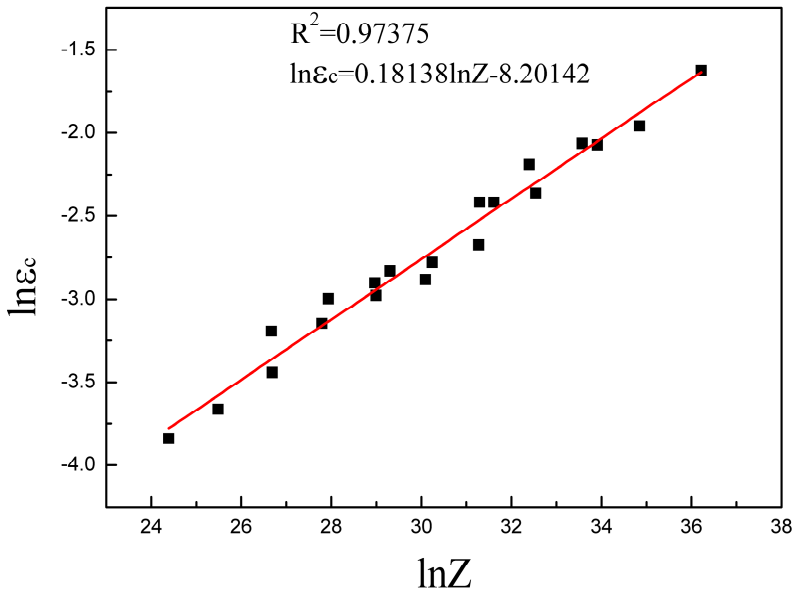

Figure 7. The relationship between the Z parameter and ε_c. The linear curve is obtained from linear fitting. Here, the Z parameter is in the form of $Z = \dot{\varepsilon}\exp(383094/(8.31T))$.

5.2.3. Description of Fractional Softening

When deformed in part II, the DRX process initiates, and the restoration process is mainly a combination of DRX and DRV. The microstructures are divided into two regions in the part: the recrystallized regions and un-recrystallized regions. As presented in Equation (5), the dislocation density ρ_r of un-recrystallized regions depends on the strain. Here, all the recrystallized regions in part II and part III are supposed to own same dislocation density ρ_{ds}. Then, the average dislocation density ρ can be expressed as follows:

$$\rho = X\rho_{ds} + (1 - X)\rho_r \tag{13}$$

Combined with Equation (6), Equation (13) can be rewritten as follows:

$$\sigma^2 = X\sigma_{ds}^2 + (1 - X)\sigma_r^2 \tag{14}$$

Through the deduction of Equation (14), the fractional softening model in hot deformation can be expressed as follows:

$$X = \frac{\sigma^2 - \sigma_r^2}{\sigma_{ds}^2 - \sigma_r^2} \tag{15}$$

The expression of Equation (15) is different from previous models. For example, as employed by Jonas et al., Serajzadeh et al. and Yang et al., fractional softening is expressed as: $X = (\sigma - \sigma_r)/(\sigma_{ds} - \sigma_{rs})$, $X = (\sigma - \sigma_p)/(\sigma_{ds} - \sigma_p)$ and $X = (\sigma^2 - \sigma_{rs}^2)/(\sigma_{ds}^2 - \sigma_{rs}^2)$, respectively [27,31,32]. In these former expressions, the strain effect on the hardening process of un-recrystallized regions is neglected or not accurately considered, which reduces the reliability of these expressions. Equation (15) is constructed by taking into account the strain effect on the hardening process; meanwhile, the relation (shown in Equation (8)) between σ_r and ε is used to describe the strain-hardening process. Taking Equation (8) into Equation (15), the fractional softening model is expressed as follows:

$$X = \frac{\sigma^2 - \sigma_y^2\exp(-k\varepsilon) - \sigma_{rs}^2[1 - \exp(-k\varepsilon)]}{\sigma_{ds}^2 - \sigma_y^2\exp(-k\varepsilon) - \sigma_{rs}^2[1 - \exp(-k\varepsilon)]} \tag{16}$$

Equation (16) is employed to describe fractional softening in this paper for a more accurate expression.

5.2.4. Determination of Avrami Constant k^* and Time Exponent n^*

As discussed above, through some proper modifications presented in Equation (11), the Avrami equation can be used to describe the DRX process. When using the modified Avrami equation for the DRX process, the expressions of $k^* = k^*(\dot{\varepsilon}, T)$ and $n^* = n^*(\dot{\varepsilon}, T)$ must be determined. Taking the natural logarithm twice on both sides of Equation (11), the following can be obtained:

$$\ln k^* + n^* \ln\left(\frac{\varepsilon - \varepsilon_c}{\dot{\varepsilon}}\right) = \ln\left(\ln\left(\frac{1}{1-X}\right)\right) \tag{17}$$

As shown in Equation (17), $\ln((\varepsilon - \varepsilon_c)/\dot{\varepsilon})$ and $\ln(\ln(1/(1-X)))$ present a linear relationship where n^* and $\ln k^*$ serve as the slope and intercept, respectively. As shown in Figure 8, $\ln((\varepsilon - \varepsilon_c)/\dot{\varepsilon})$ vs. $\ln(\ln(1/(1-X)))$ curves are employed to determine the values of n^* and k^* at different temperatures and strain rates for Armco-type pure iron. Here, the recrystallized volume fraction X in these curves is calculated via Equation (16). The values of n^* and $\ln k^*$, obtained from the linear fitting, are presented in the Supplementary Materials of Table S2. As discussed above, k^* and n^* are supposed to be the function of T and $\dot{\varepsilon}$. Whether $\dot{\varepsilon}$ and T show combined effects (e.g., in the form of the Z parameter) or individual effects on k^* and n^* also needs to be discussed.

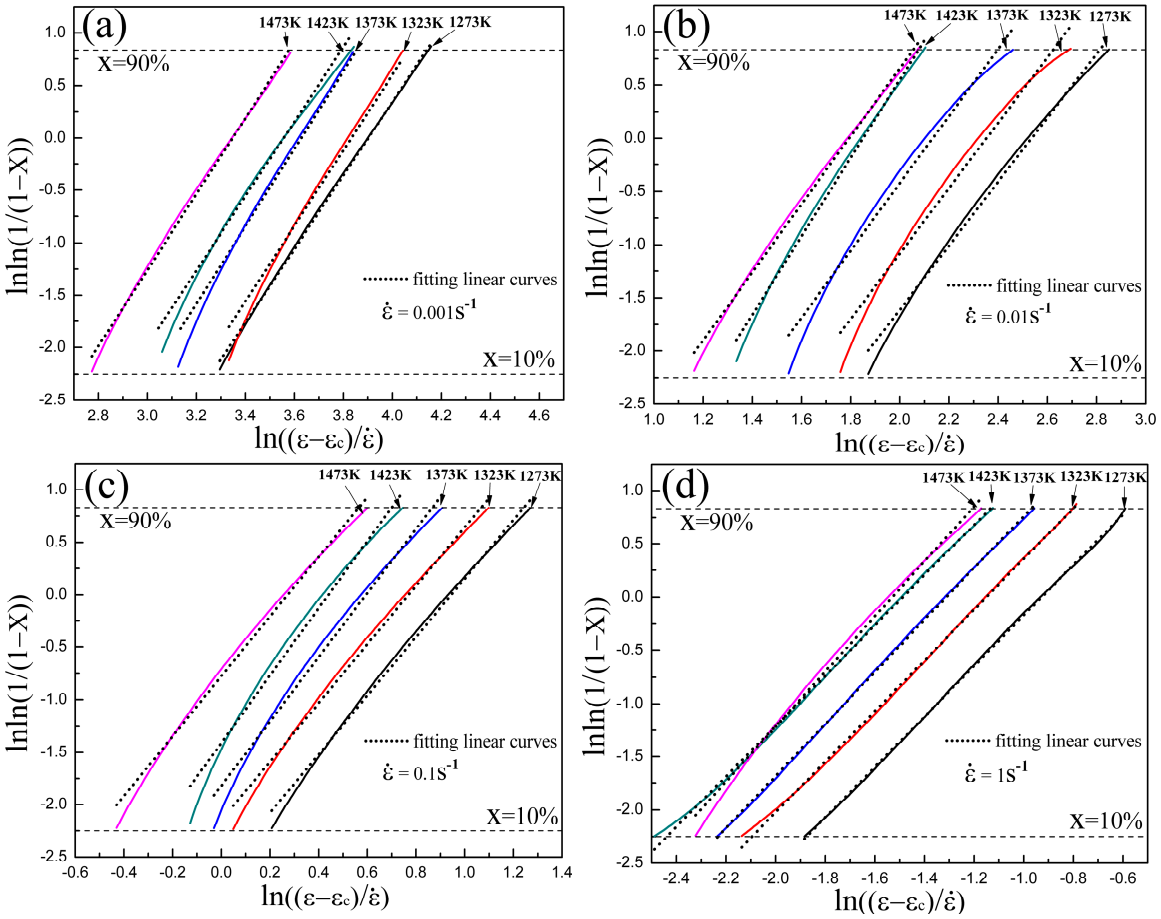

Figure 8. $\ln(\ln(1/(1-X)))$ vs. $\ln((\varepsilon - \varepsilon_c)/\dot{\varepsilon})$ curves of Armco-type pure iron: (**a**) $\dot{\varepsilon}$ = 0.001 s^{-1}; (**b**) $\dot{\varepsilon}$ = 0.01 s^{-1}; (**c**) $\dot{\varepsilon}$ = 0.1 s^{-1}; and (**d**) $\dot{\varepsilon}$ = 1 s^{-1}. The values of X are calculated out through Equation (16). The dot lines are the linear fitting results of each curve. After the linear fitting, n_1 and $\ln k^*$ are obtained as the slope and intercept, respectively.

As shown in Figure 8, the values of the slope n^* are nearly the same when in the same strain rates; meanwhile, the temperatures show no obvious effects. Here, the average values of n^* for strain rates of 0.001 s^{-1}, 0.01 s^{-1}, 0.1 s^{-1} and 1 s^{-1} are 3.595144, 3.224808, 2.939272 and 2.43113, respectively. The relation between the average values and $\dot{\varepsilon}$ shown in Figure 9 is employed to determine the expression: $n^* = n^*(\dot{\varepsilon})$. Through a linear fitting, $n^*(\dot{\varepsilon})$ is obtained as follows:

$$n^* = -0.16406 \ln \dot{\varepsilon} + 2.48095 \quad (18)$$

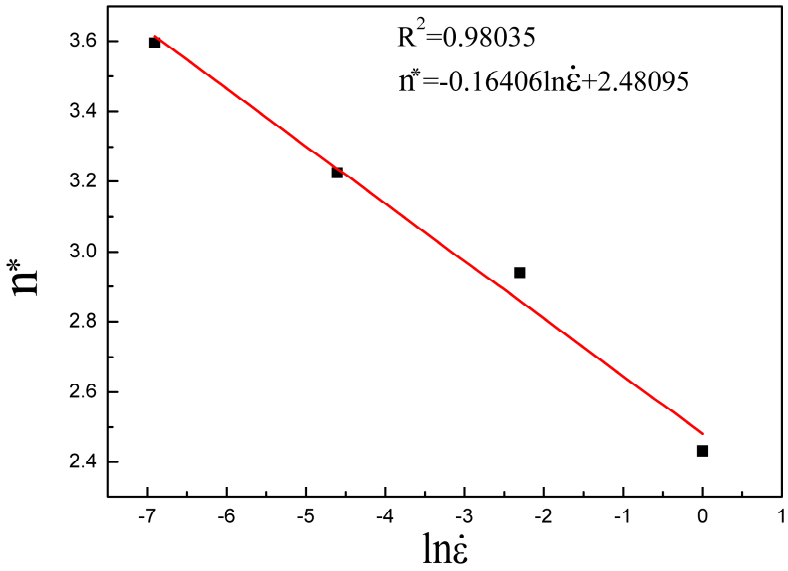

Figure 9. The relationship between n^* and $\dot{\varepsilon}$. The linear curve is obtained from linear fitting.

The relation between k^* and Z shown in Figure 10 is employed to determine the expression: $k^* = k^*(\dot{\varepsilon}, T)$. As shown in the figure, $\ln k^*$ and $\ln Z$ present a linear relationship when in the same strain rates. The slopes of these linear fitting curves are supposed to be same, and the average value is -0.3484. However, the intercepts are different, and the intercepts for strain rates of 0.001 s^{-1}, 0.01 s^{-1}, 0.1 s^{-1} and 1 s^{-1} are -3.89581, 2.99362, 9.56383 and 14.89145, respectively. Therefore, except for the combined effects of T and $\dot{\varepsilon}$ on k^* in the form of the Z parameter, $\dot{\varepsilon}$ also shows an individual effect, and $k^* = k^*(\dot{\varepsilon}, T)$ can be expressed as follows:

$$\ln k^* = -0.3484 \ln Z + f(\dot{\varepsilon}) \quad (19)$$

where $f(\dot{\varepsilon})$ is the function representing the individual effect of the strain rate. The relation between the intercepts and strain rate inserted in Figure 10 is employed to determine the expression of $f(\dot{\varepsilon})$. Through a linear fitting, $f(\dot{\varepsilon})$ is obtained as follows:

$$f(\dot{\varepsilon}) = 2.7331 \ln \dot{\varepsilon} + 15.32807 \quad (20)$$

Taking Equation (20) into Equation (19), k^* can be expressed as follows:

$$k^* = Z^{-0.3484} \exp(2.7331 \ln \dot{\varepsilon} + 15.32807) \quad (21)$$

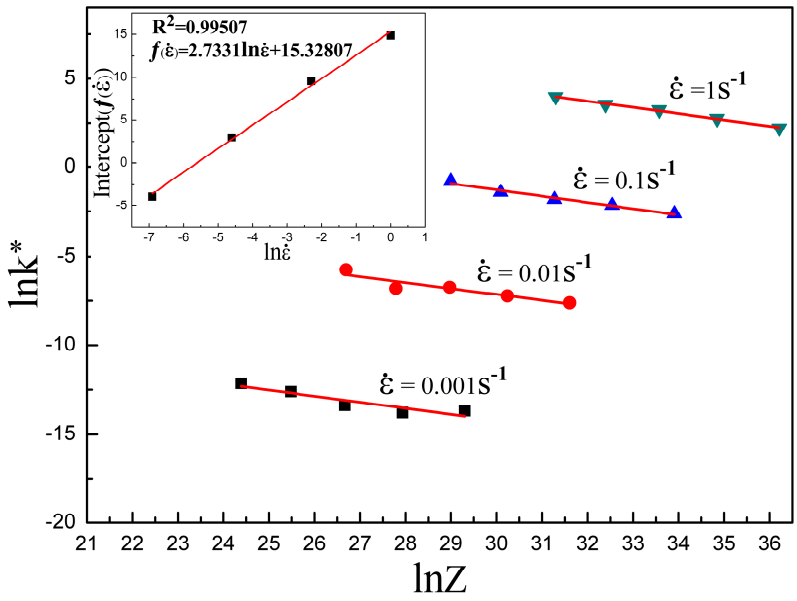

Figure 10. The relationship between the Z parameter and k^*. These linear curves are obtained from the linear fitting of points with the same strain rates. Here, the Z parameter is in the form of $Z = \dot{\varepsilon}\exp(383094/(8.31T))$. Insert: the relationship between $\dot{\varepsilon}$ and the intercepts of these linear fitting curves.

5.2.5. Constitutive Models Relating to the DRX and DRV Processes

Combined of Equations (11), (12), (18) and (21), the Avrami kinetic equation for Armco-type pure iron is expressed as follows:

$$\begin{cases} X = 1 - \exp\left[-k^*\left(\frac{\varepsilon-\varepsilon_c}{\dot{\varepsilon}}\right)^{n^*}\right] \\ \varepsilon_c = 2.74264 \times 10^{-4} Z^{0.18138} \\ n^* = -0.16406 \ln\dot{\varepsilon} + 2.48095 \\ k^* = Z^{-0.3484}\exp(2.7331\ln\dot{\varepsilon} + 15.32807) \end{cases} \quad (22)$$

The DRX process of Armco-type pure iron can be well described through Equation (22), which presents the influences of strain, strain rate and temperature on the DRX process. The S-curves of Armco-type pure iron are calculated out by Equation (22) and presented in Figure 11. As shown in the figure, when in same strain, the volume fraction of DRX increases with an increasing temperature and decreasing strain rate. Meanwhile, the critical strain of DRX increases with a decreasing temperature and increasing strain rate.

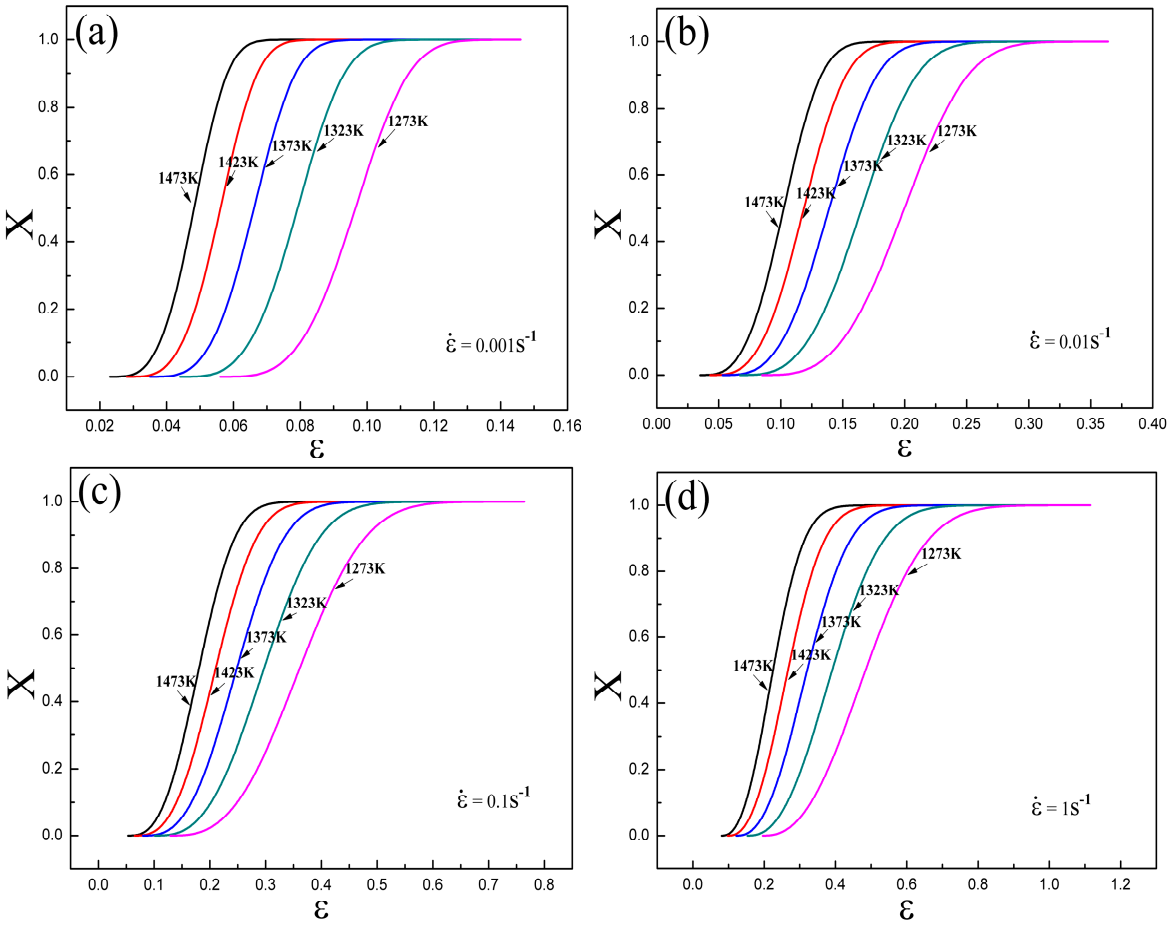

Figure 11. S-curves of Armco-type pure iron calculated by Equation (22): (**a**) $\dot{\varepsilon}$ = 0.001 s^{-1}; (**b**) $\dot{\varepsilon}$ = 0.01 s^{-1}; (**c**) $\dot{\varepsilon}$ = 0.1 s^{-1}; and (**d**) $\dot{\varepsilon}$ = 1 s^{-1}.

The constitutive relationship for alloys in hot deformation refers to the DRV process (un-recrystallized regions) and DRX process. The relation between these two processes can be described through Equation (14). Meanwhile, the DRV process can be described by Equation (8). Taking Equation (8) into Equation (14), the constitutive model for alloys in hot deformation can be expressed as follows:

$$\sigma = \left\{ X\sigma_{ds}^2 + (1-X)\sigma_y^2 \exp(-k\varepsilon) + (1-X)\sigma_{rs}^2[1-\exp(-k\varepsilon)] \right\}^{1/2} \quad (23)$$

For Armco-type pure iron, k and X are expressed by Equations (9) and (22), respectively. Through Equation (23) and the values of σ_{ds}, σ_y and σ_{rs} provided in the Supplementary Materials of Table S2, the true stress-strain curves of Armco-type pure iron are calculated out and presented in Figure 12. As shown in the figure, these calculated curves fit well with the original true stress-strain curves in whole part, which means the flow behavior of alloys in hot deformation can be well described through Equation (23). However, the initial values of σ_{ds}, σ_y and σ_{rs} used in Equation (23) have all been obtained from polynomial fitting. For the completion of Equation (23), it is meaningful to determine the expressions of σ_{ds}, σ_y and σ_{rs}.

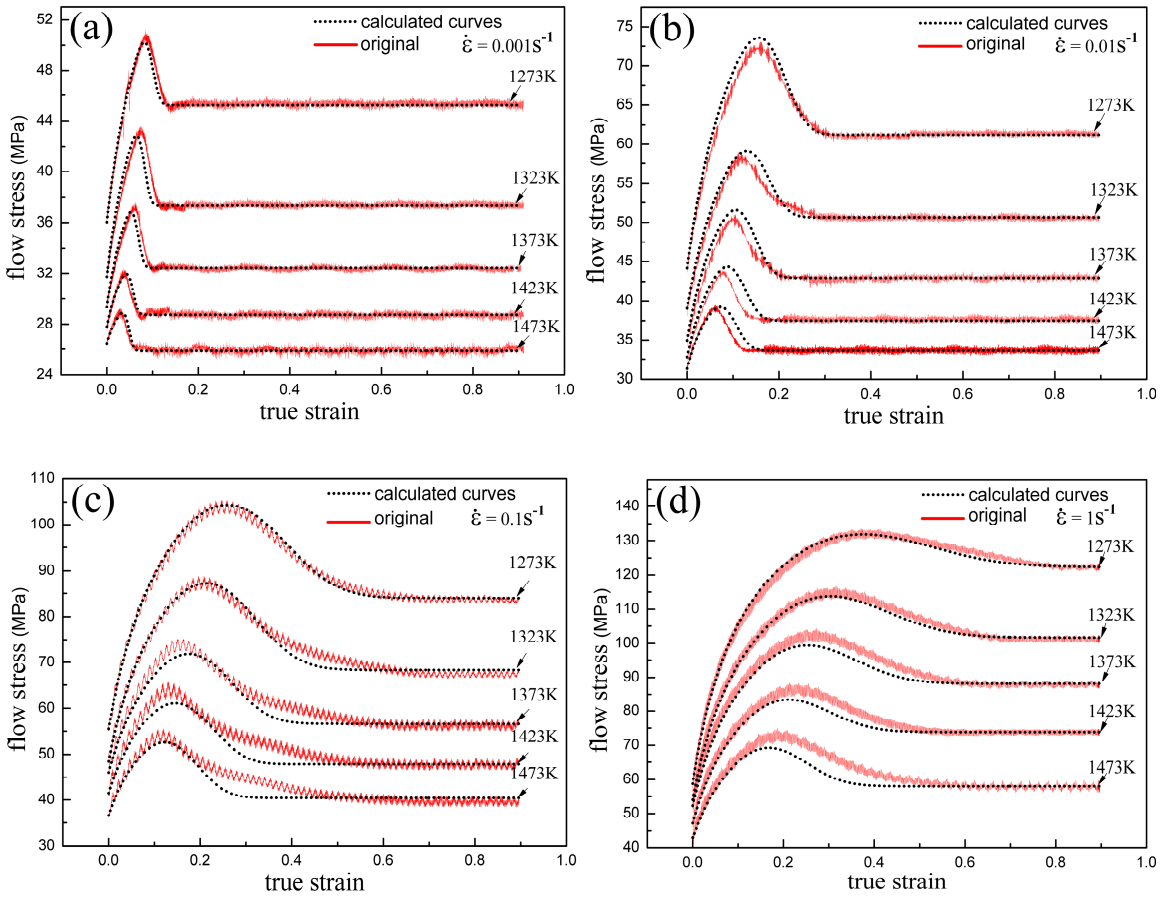

Figure 12. Original true stress-strain curves and calculated flow stress curves considering eDRV and DRX processes of Armco-type pure iron: (**a**) $\dot{\varepsilon} = 0.001\ s^{-1}$; (**b**) $\dot{\varepsilon} = 0.01\ s^{-1}$; (**c**) $\dot{\varepsilon} = 0.1\ s^{-1}$; and (**d**) $\dot{\varepsilon} = 1\ s^{-1}$. The red solid curves are the original true stress-strain curves while the dot lines are the flow stress curves calculated through Equation (23).

5.3. Constitutive Relationship of Part III

5.3.1. Constitutive Model of Part III

When deformed in part III, the flow stress reaches a steady state σ_{ds}, and all the original microstructures are completely recrystallized. Beladi et al. and Graetz et al. proposed that the recrystallized grain size is decreased as long as the strain rate increases and the temperature decreases, which is independent of the initial grain size and strain [21,22]. As discussed above, the precision of Arrhenius-type equations is reduced due to the neglect of the strain effects. However, the strain effects need no consideration when in a steady state where the flow stress is independent of the strain; therefore, using Arrhenius-type equations to describe the flow behavior of the steady state is appropriate. According to different hot deformation conditions, Arrhenius-type equations based of the Z parameter can be expressed as follows:

$$Z = f(\sigma_{ds}) = A_1 {\sigma_{ds}}^{n_1} \quad (24)$$

$$Z = f(\sigma_{ds}) = A_2 \exp(\beta \sigma_{ds}) \quad (25)$$

$$Z = f(\sigma_{ds}) = A[\sinh(\alpha \sigma_{ds})]^n \quad (26)$$

The stress multiplier α is defined as: $\alpha = \beta / n_1$. As proposed by Mandal et al. and Lin et al., Equation (24) is preferred for a low strain level where $\alpha\sigma_{ds} < 0.8$, while Equation (25) is preferred for a high strain level where $\alpha\sigma_{ds} > 1.2$ [33,34]. The sine-hyperbolic equation of Equation (26), proposed

by Sellars et al., is widely employed to describe the relationship between flow stress, strain rate and deformation temperature over a wide range of stresses [14]. Therefore, Equation (26) is used to describe the flow behavior of the steady state in this work. According to Equation (26), the constitutive model for part III can be expressed as follow:

$$\sigma_{ds} = \frac{1}{\alpha} \ln\left\{ \left(\frac{Z}{A}\right)^{1/n} + \left[\left(\frac{Z}{A}\right)^{2/n} + 1 \right]^{1/2} \right\} \tag{27}$$

5.3.2. Determination of Constants α, n and Q

Taking the natural logarithm of both sides of Equations (24), (25) and (26), the following forms can be obtained:

$$\ln Z = \ln \dot{\varepsilon} + \frac{Q_1}{RT} = \ln A_1 + n_1 \ln \sigma_{ds} \tag{28}$$

$$\ln Z = \ln \dot{\varepsilon} + \frac{Q_2}{RT} = \ln A_2 + \beta \sigma_{ds} \tag{29}$$

$$\ln Z = \ln \dot{\varepsilon} + \frac{Q}{RT} = \ln A + n \ln[\sinh(\alpha \sigma_{ds})] \tag{30}$$

With respect to temperature, the partial differentiations of Equations (28), (29) and (30) yield the following:

$$n_1 = \left. \frac{\partial \ln \dot{\varepsilon}}{\partial \ln \sigma_{ds}} \right|_T \tag{31}$$

$$\beta = \left. \frac{\partial \ln \dot{\varepsilon}}{\partial \sigma_{ds}} \right|_T \tag{32}$$

$$n = \left. \frac{\partial \ln \dot{\varepsilon}}{\partial \ln[\sinh(\alpha \sigma_{ds})]} \right|_T \tag{33}$$

With respect to the strain rate, the partial differentiation of Equation (30) yields the following:

$$Q = Rn \left. \frac{\partial \ln[\sin(\alpha \sigma_{ds})]}{\partial (1/T)} \right|_{\dot{\varepsilon}} \tag{34}$$

The values of σ_{ds} presented in the Supplementary Materials of Table S1, and the corresponding strain rates and temperatures, are used to determine the values of these constants. As shown in Figure 13, using the linear regression of these data, the values of n_1, β and n obtained as the average slopes of $\ln \dot{\varepsilon}$-$\ln \sigma_{ds}$, $\ln \dot{\varepsilon}$-σ_{ds} and $\ln \dot{\varepsilon}$-$\ln[\sinh(\alpha \sigma_{ds})]$, are 7.37182, 0.13345 and 5.50432, respectively. Meanwhile, the value of α obtained as the average value of β/n_1 is 0.01777, and the value of Q calculated based on the average slopes of $\ln[\sinh(\alpha \sigma_{ds})]$-$1/T$ is 383094 J mol^{-1}. The activation energy of Armco-type pure iron is lower than that of other steels, and this is mainly caused by the high Fe atom purity. Alloy elements in other steels usually decrease the mobility of Fe atoms and thus increase the value of Q. According to the calculated value of Q, the Z parameter for Armco-type pure iron can be expressed as follows:

$$Z = \dot{\varepsilon} \exp\left(\frac{383094}{8.31T}\right) \tag{35}$$

According to Equation (30) the value of $\ln A$ can be gained as the intercept of the $\ln(Z) - \ln[\sinh(\alpha \sigma_{ds})]$ plot. Through the linear regression shown in Figure 14, the value of $\ln A$ is 29.6307, and A is 7.38668×10^{12}. Taking the values of α, n and A into Equation (27), the constitutive model for Armco-type pure iron in part III can be expressed as follows:

$$\sigma_{ds} = \frac{1}{0.01777}\ln\left\{\left(\frac{Z}{7.38668\times10^{12}}\right)^{1/5.50432} + \left[\left(\frac{Z}{7.38668\times10^{12}}\right)^{2/5.50432} + 1\right]^{1/2}\right\} \quad (36)$$

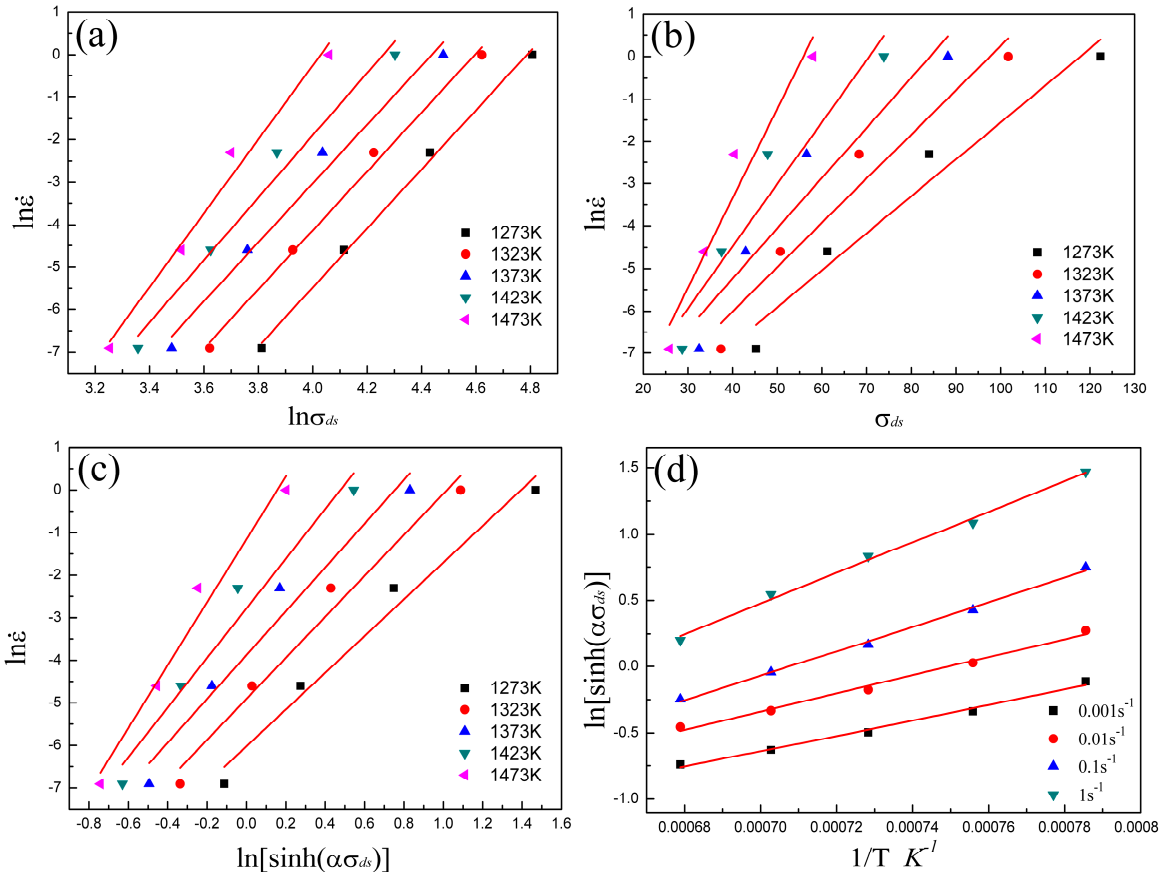

Figure 13. The relationships between $\dot{\varepsilon}$, σ_{ds} and T: (**a**) $\ln\dot{\varepsilon}$ and $\ln\sigma_{ds}$; (**b**) $\ln\dot{\varepsilon}$ and σ_{ds}; (**c**) $\ln\dot{\varepsilon}$ and $\ln[\sinh(\alpha\sigma_{ds})]$; and (**d**) $\ln[\sinh(\alpha\sigma_{ds})]$ and $1/T$. The linear curves are obtained from linear fitting.

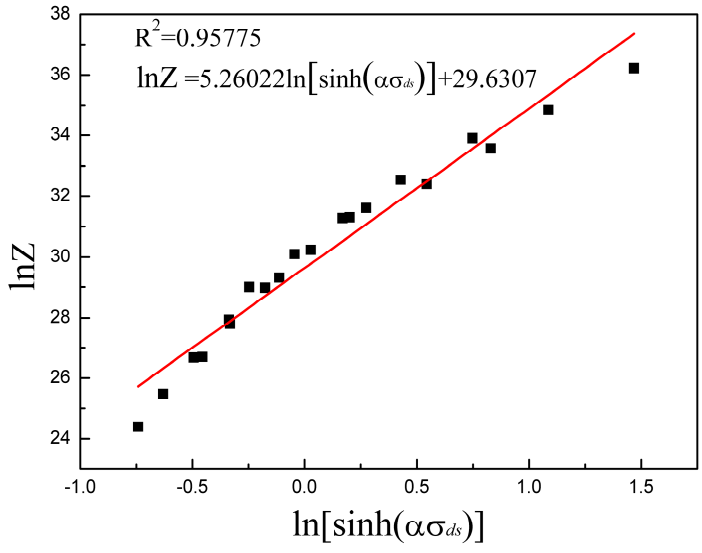

Figure 14. Relationship between Z parameter and σ_{ds}. The linear curve is got from linear fitting.

5.4. Integrated Constitutive Relationship for Hole Part

5.4.1. Determination of Yield Stress σ_y and Saturation Stress σ_{rs}

Figure 15 presents the relations between σ_y, σ_{rs} and the Z parameter. Shown in the figure, $\dot{\varepsilon}$ and T show combined effects on σ_y and σ_{rs} in the form of the Z parameter. Meanwhile, σ_y and σ_{rs} present linear relations with ln Z. Through linear fitting, the expressions of σ_y and σ_{rs} for Armco-type pure iron can be expressed as follows:

$$\sigma_y = 3.00921 \ln Z - 50.0975 \tag{37}$$

$$\sigma_{rs} = 9.69716 \ln Z - 218.049 \tag{38}$$

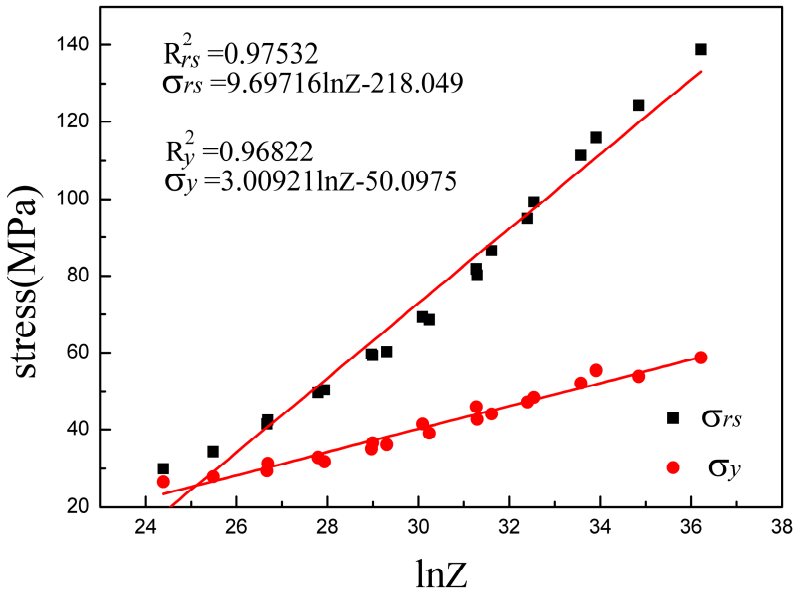

Figure 15. The relationships between σ_y, σ_{rs} and the Z parameter. The linear curves are obtained from linear fitting.

5.4.2. Avrami Kinetic-Based Constitutive Model of Whole Part

Integrating expressions of Equations (11) and (23), the Avrami kinetic-based constitutive model for alloys considering the effects of DRV and DRX can be expressed as follows:

$$\begin{cases} \sigma = \left\{ X\sigma_{ds}^2 + (1-X)\sigma_y^2 \exp(-k\varepsilon) + (1-X)\sigma_{rs}^2[1-\exp(-k\varepsilon)] \right\}^{1/2} \\ X = \begin{cases} 0 & for \quad \varepsilon \le \varepsilon_c \\ 1-\exp\left[-k^*\left(\frac{\varepsilon-\varepsilon_c}{\dot{\varepsilon}}\right)^{n^*}\right] & for \quad \varepsilon \ge \varepsilon_c \end{cases} \end{cases} \tag{39}$$

As discussed above for Armco-type pure iron, σ_{ds}, σ_y, σ_{rs}, k, ε_c, k^* and n^* are expressed as follows:

$$\begin{cases} \sigma_{ds} = \frac{1}{0.01777}\ln\left\{\left(\frac{Z}{7.38668\times10^{12}}\right)^{1/5.50432}+\left[\left(\frac{Z}{7.38668\times10^{12}}\right)^{2/5.50432}+1\right]^{1/2}\right\} \\ \sigma_y = 3.00921\ln Z - 50.0975 \\ \sigma_{rs} = 9.69716\ln Z - 218.049 \\ k = \exp\left[0.01723(\ln Z)^2 - 1.18699(\ln Z) + 22.28195\right] \\ \varepsilon_c = 2.74264\times10^{-4}Z^{0.18138} \\ n^* = -0.16406\ln\dot{\varepsilon} + 2.48095 \\ k^* = Z^{-0.3484}\exp(2.7331\ln\dot{\varepsilon} + 15.3281) \\ Z = \dot{\varepsilon}\exp\left(\frac{383094}{8.31T}\right) \end{cases} \quad (40)$$

Using Equations (39) and (40), the flow behavior of Armco-type pure iron is well described, and the flow stress curves calculated out through these two equations are presented in Figure 16. As shown in the figure, the strain effects are considered, especially for these parts before the steady state; meanwhile, the DRV and DRX characters referring to strain hardening, and the stress peak are well presented in these curves.

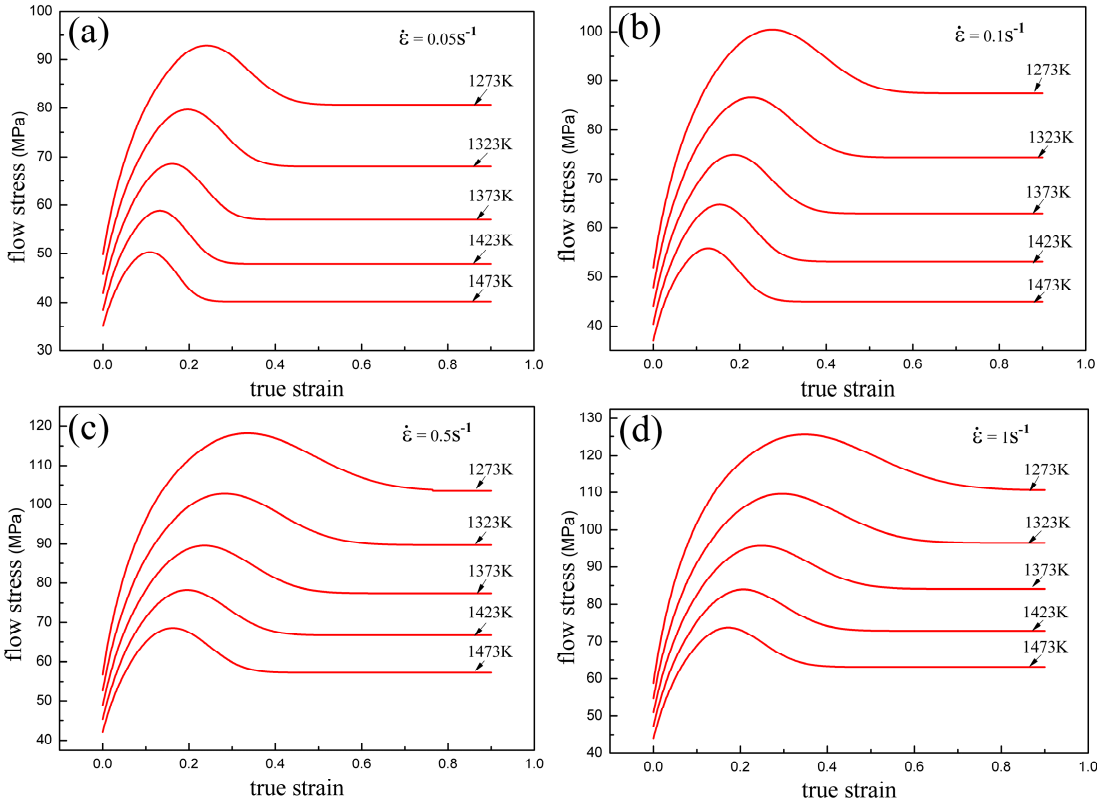

Figure 16. Calculated flow stress curves using the Avrami kinetic-based constitutive model of Armco-type pure iron: (**a**) $\dot{\varepsilon}$ = 0.05 s^{-1}; (**b**) $\dot{\varepsilon}$ = 0. 1 s^{-1}; (**c**) $\dot{\varepsilon}$ = 0.5 s^{-1}; and (**d**) $\dot{\varepsilon}$ = 1 s^{-1}.

6. Conclusions

The work presents a full mathematical description of the stress-strain compression curves in a wide range of strain rates and deformation temperatures. The constructed models are based on the dislocation structure evolution equation (in the case of DRV) and Avrami kinetic-based model (in the case of DRX). Based on this study, the following can be concluded:

(1) Based on the KM model, the strain-hardening process relating only to DRV can be described by the equation: $\sigma_r{}^2 = \sigma_y^2 \exp(-k\varepsilon) + \sigma_{rs}^2[1 - \exp(-k\varepsilon)]$. σ_{rs} is determined by the part of the true stress-strain curve before the initiation of DRX. As for Armco-type pure iron, $\dot{\varepsilon}$ and T show combined effects on k, σ_y and σ_{rs} in the form of the Z parameter with expressions as: $k = \exp\left[0.01723(\ln Z)^2 - 1.18699(\ln Z) + 22.28195\right]$, $\sigma_y = 3.00921 \ln Z - 50.0975$ and $\sigma_{rs} = 9.69716 \ln Z - 218.049$, respectively.

(2) Considering the strain-hardening process, the model used to describe the fractional softening for alloys under DRX is modified as: $X = (\sigma^2 - \sigma_r^2)/(\sigma_{ds}^2 - \sigma_r^2)$. The volume fraction of DRX increases as long as the temperature increases and the strain rate decreases. The critical points for the onset of DRX are determined as the inflection point in the θ vs. σ curve. As for Armco-type pure iron, the relation between ε_c and the Z parameter is expressed as: $\varepsilon_c = 2.74264 \times 10^{-4} Z^{0.18138}$.

(3) The Avrami kinetic equation is used to describe the kinetic of DRX with the modified expression as: $X = 1 - \exp\left[-k^*\left((\varepsilon - \varepsilon_c)/\dot{\varepsilon}\right)^{n^*}\right]$, where $k^* = k^*(\dot{\varepsilon}, T)$ and $n^* = n^*(\dot{\varepsilon}, T)$. As for Armco-type pure iron, including an individual effect, the strain rate $\dot{\varepsilon}$ also presents a combined effect with T on k^* in the form of the Z parameter, and the relation is expressed as: $k^* = Z^{-0.3484} \exp(2.7331 \ln \dot{\varepsilon} + 15.32807)$. n^* is only the function of $\dot{\varepsilon}$ with the expression: $n^* = -0.16406 \ln \dot{\varepsilon} + 2.48095$.

(4) Arrhenius-type equations are suitable for describing the flow behavior of the steady state. Regressing from the equations, the DRX activation energy for Armco-type pure iron is 383094 J mol^{-1}, and the expressions for the Z parameter and σ_{ds} are determined as Equations (35) and (36), respectively.

(5) Based on strain hardening, fractional softening models and the modified Avrami kinetic equation, the constitutive model for alloys considering the effects of DRV and DRX is constructed as Equation (39). The constitutive model can be well used to describe the flow behavior of Armco-type pure iron. The DRV and DRX characters are clearly presented in these curves determined by this model.

Supplementary Materials: The following are available online at http://www.mdpi.com/2075-4701/9/3/365/s1, Table S1. Fitted values of Armco-type pure iron; Table S2. Calculated values of Armco-type pure iron.

Author Contributions: Conceptualization, Q.F. and Y.Z.; methodology, Y.Z.; software, Y.Z.; validation, Y.Z.; formal analysis, Y.Z.; investigation, Y.Z.; resources, X.Z.; data curation, Y.Z.; writing—original draft preparation, Y.Z.; writing—review and editing, Y.Z.; visualization, Y.Z.; supervision, Z.Z. project administration, Z.X.; funding acquisition, Z.Q.

Funding: This research received no external funding.

Acknowledgments: Thanks for the support from my love, my family and group colleagues.

Conflicts of Interest: The authors declare no conflict of interest. The funders had no role in the design of the study; in the collection, analyses, or interpretation of data; in the writing of the manuscript, or in the decision to publish the results.

Nomenclature

$\dot{\varepsilon}$	strain rate (s^{-1})
T	temperature (K)
Q	activation energy (J mol^{-1})
R	universal gas constant (8.31 J $mol^{-1}K^{-1}$)
Z	Zener–Hollomon parameter
ε	strain
ε_y	yield strain
ε^*	strain at maximum softening rate
ε_c, σ_c	critical strain and critical stress (MPa)
ε_p, σ_p	peak strain and peak stress (MPa)
σ, σ_{ds}	flow stress (MPa) and steady value of it
σ_r, σ_{rs}	recovery stress (MPa) and saturation value of it
ρ	average dislocation density corresponding to whole deforming process
ρ_r	dislocation density corresponding to only DRV process
ρ_y	dislocation density at yield point
ρ_{ds}	dislocation density at the steady state of flow stress
ρ_{rs}	dislocation density at the saturation state of recovery stress
G	shear modulus
b	burgers vector
X	recrystallized volume fraction
k^*	Avrami constant
t	time (s)
t_{50}	characteristic time
n^*	time exponent
d	grain size
A, A_1, A_2, α, β, n, n_1, k, k_1, a^*, A', q, v	constants

References

1. McQueen, H.J.; Ryan, N.D. Constitutive analysis in hot working. *Mater. Sci. Eng. A* **2002**, *322*, 43–63. [CrossRef]
2. He, Z.B.; Wang, Z.B.; Lin, Y.L.; Fan, X.B. Hot Deformation behavior of a 2024 aluminum alloy sheet and its modeling by Fields-Backofen model considering strain rate evolution. *Metals* **2019**, *9*, 243. [CrossRef]
3. Salinas, A.; Celentano, D.; Carvajal, L.; Artigas, A.; Monsalve, A. Microstructure-Based Constitutive Modelling of Low-Alloy Multiphase TRIP Steels. *Metals* **2019**, *9*, 250. [CrossRef]
4. Zener, C.; Hollomon, J.H. Effect of strain rate upon plastic flow of steel. *J. Appl. Phys.* **1944**, *15*, 22–32. [CrossRef]
5. Johnson, G.R.; Cook, W.H. Fracture characteristics of three metals subjected to various strains, strain rates, temperatures and pressures. *Eng. Fract. Mech.* **1985**, *21*, 31–48. [CrossRef]
6. Ulacia, I.; Salisbury, C.P.; Hurtado, I.; Worswick, M.J. Tensile characterization and constitutive modeling of AZ31B magnesium alloy sheet over wide range of strain rates and temperatures. *J. Mater. Process. Technol.* **2011**, *211*, 830–839. [CrossRef]
7. Bhattacharya, R.; Lanc, Y.J.; Wynne, B.P.; Davis, B.; Rainforth, W.M. Constitutive equations of flow stress of magnesium AZ31 under dynamically recrystallizing conditions. *J. Mater.Process. Technol.* **2014**, *214*, 1408–1417. [CrossRef]
8. Gambirasio, L.; Rizzi, E. On the calibration strategies of the Johnson–Cook strength model: Discussion and applications to experimental data. *Mater. Sci. Eng. A* **2014**, *610*, 370–413. [CrossRef]
9. Zerilli, F.J.; Armstrong, R.W. Dislocation-mechanics-based constitutive relations for material dynamics calculations. *J. Appl. Phys.* **1987**, *61*, 1816–1825. [CrossRef]
10. Estrin, Y.; Mecking, H. A unified phenomenological description of work hardening and creep based on one-parameter models. *Acta Metall.* **1984**, *32*, 57–70. [CrossRef]
11. Choudhary, B.K.; Christopher, J. Comparative tensile flow and work-hardening behavior of 9 Pct chromium ferritic-martensitic steels in the framework of the Estrin-Mecking internal-variable approach. *Metall. Mater. Trans. A* **2016**, *47*, 2642–2655. [CrossRef]

12. Haghdadi, N.; Martin, D.; Hodgson, P. Physically-based constitutive modeling of hot deformation behavior in a LDX 2101 duplex stainless steel. *Mater. Des.* **2016**, *106*, 420–427. [CrossRef]
13. Chalimba, S.A.; Mostert, R.; Stumpf, W.; Siyasiya, C.; Banks, K. Modeling of work hardening during hot rolling of vanadium and niobium microalloyed steels in the low temperature austenite region. *J. Mater. Eng. Perform.* **2017**, *26*, 5217–5227. [CrossRef]
14. Sellars, C.M.; Tegart, W.M. On the mechanism of hot deformation. *Acta Metall.* **1966**, *14*, 1136–1138. [CrossRef]
15. Li, J.D.; Liu, J.S. Strain Compensation Constitutive Model and Parameter Optimization for Nb-Contained 316LN. *Metals* **2019**, *9*, 212. [CrossRef]
16. Tabei, A.; Abed, F.H.; Voyiadjis, G.Z.; Garmestani, H. Constitutive modeling of Ti-6Al-4V at a wide range of temperatures and strain rates. *Eur. J. Mech.-A/Solids* **2017**, *63*, 128–135. [CrossRef]
17. Zhang, C.S.; Ding, J.; Dong, Y.Y.; Zhao, G.Q.; Gao, A.J.; Wang, L.J. Identification of friction coefficients and strain-compensated Arrhenius-type constitutive model by a two-stage inverse analysis technique. *Int. J. Mech. Sci.* **2015**, *98*, 195–204. [CrossRef]
18. Kugler, G.; Turk, R. Modeling the dynamic recrystallization under multi-stage hot deformation. *Acta Mater.* **2004**, *52*, 4659–4668. [CrossRef]
19. Martin, E.; Jonas, J.J. Evolution of microstructure and microtexture during the hot deformation of Mg–3% Al. *Acta Mater.* **2010**, *58*, 4253–4266. [CrossRef]
20. Tian, B.; Lind, C.; Schafler, E.; Paris, O. Evolution of microstructures during dynamic recrystallization and dynamic recovery in hot deformed Nimonic 80a. *Mater. Sci. Eng. A* **2004**, *367*, 198–204. [CrossRef]
21. Beladi, H.; Cizek, P.; Hodgson, P.D. On the characteristics of substructure development through dynamic recrystallization. *Acta Mater.* **2010**, *58*, 3531–3541. [CrossRef]
22. Graetz, K.; Miessen, C.; Gottstein, G. Analysis of steady-state dynamic recrystallization. *Acta Mater.* **2014**, *67*, 58–66. [CrossRef]
23. Haghdadi, N.; Cizek, P.; Beladi, H.; Hodgson, P.D. The austenite microstructure evolution in a duplex stainless steel subjected to hot deformation. *Philos. Mag.* **2017**, *97*, 1209–1237. [CrossRef]
24. Babu, K.A.; Mandal, S.; Athreya, C.N.; Shakthipriya, B.; Sarma, V.S. Hot deformation characteristics and processing map of a phosphorous modified super austenitic stainless steel. *Mater. Des.* **2017**, *115*, 262–275. [CrossRef]
25. Avrami, M. Kinetics of phase change. I. General theory. *J. Chem. Phys.* **1939**, *7*, 1103–1112. [CrossRef]
26. Avrami, M. Kinetics of phase change. II. Transformation-time relations for random distribution of nuclei. *J. Chem. Phys.* **1940**, *8*, 212–224. [CrossRef]
27. Jonas, J.J.; Quelennec, X.; Jiang, L.; Martin, E. The Avrami kinetics of dynamic recrystallization. *Acta Mater.* **2009**, *57*, 2748–2756. [CrossRef]
28. Kim, S.I.; Yoo, Y.C. Dynamic recrystallization behavior of AISI 304 stainless steel. *Mater. Sci. Eng. A* **2001**, *311*, 108–113. [CrossRef]
29. Quan, G.Z.; Wu, D.S.; Luo, G.C.; Xia, Y.F.; Zhou, J.; Liu, Q.; Gao, L. Dynamic recrystallization kinetics in α phase of as-cast Ti–6Al–2Zr–1Mo–1V alloy during compression at different temperatures and strain rates. *Mater. Sci. Eng. A* **2014**, *589*, 23–33. [CrossRef]
30. Poliak, E.I.; Jonas, J.J. A one-parameter approach to determining the critical conditions for the initiation of dynamic recrystallization. *Acta Mater.* **1996**, *44*, 127–136. [CrossRef]
31. Serajzadeh, S.; Taheri, A.K. An investigation on the effect of carbon and silicon on flow behavior of steel. *Mater. Des.* **2002**, *23*, 271–276. [CrossRef]
32. Yang, Z.; Guo, Y.C.; Li, J.P.; He, F.; Xia, F.; Liang, M.X. Plastic deformation and dynamic recrystallization behaviors of Mg–5Gd–4Y–0.5Zn–0.5Zr alloy. *Mater. Sci. Eng. A* **2008**, *485*, 487–491. [CrossRef]
33. Mandal, S.; Rakesh, V.; Sivaprasad, P.V.; Venugopal, S.; Kasiviswanathan, K.V. Constitutive equations to predict high temperature flow stress in a Ti-modified austenitic stainless steel. *Mater. Sci. Eng. A* **2009**, *500*, 114–121. [CrossRef]
34. Lin, Y.C.; Xia, Y.C.; Chen, X.M.; Chen, M.S. Constitutive descriptions for hot compressed 2124-T851 aluminum alloy over a wide range of temperature and strain rate. *Comput. Mater. Sci.* **2010**, *50*, 227–233. [CrossRef]